PCCP

PAPER

Check for updates

Cite this: *Phys. Chem. Chem. Phys.*, 2019, **21**, 24206

Two-dimensional Dirac fermions on oxidized black phosphorus

Seoung-Hun Kang,[ab] Jejune Park,†[a] Sungjong Woo*[bc] and Young-Kyun Kwon *[ab]

Received 7th August 2019,
Accepted 17th October 2019

DOI: 10.1039/c9cp04372a

rsc.li/pccp

We explore the oxidation of a single layer of black phosphorus using *ab initio* density functional theory calculations. We search for the equilibrium structures of phosphorene oxides, PO_x with various oxygen concentrations x ($0 \leq x \leq 1$). By evaluating the formation energies with diverse configurations and their vibrational properties for each of various x values, we identify a series of stable oxidized structures with x and confirm that the oxidation occurs naturally. We also find that oxidation makes some modes from the P–O bonds and P–P bonds IR-active implying that the infrared spectra can be used to determine the degree of oxidation of phosphorene. Our electronic structure calculations reveal that the fully oxidized phosphorene (PO) has a direct band gap of 0.83 eV similar to the pristine phosphorene. Intriguingly, the PO possesses two nonsymmorphic symmetries with the inversion symmetry broken, guaranteeing symmetry-protected band structures including the band degeneracy and four-fold degenerate Dirac points. Our results provide an important guide in the search for the rare example of a Dirac semimetal with a higher level of degeneracy, giving significant insight into the relations between the symmetry of the lattice and band topology of electrons.

1 Introduction

Since its synthesis and fabrication,[1–3] a single layer of black phosphorus or phosphorene has attracted a lot of attention due to its inherent direct band gap. The energy gap varies from 1.9 eV (monolayer) to 0.3 eV (bulk) according to the number of layers.[4] Its high hole mobility and on/off ratio make phosphorene a potential candidate for future electronic devices.[1–3,5] On the other hand, it has been reported that single or few-layered phosphorene is highly reactive with air, especially, in an oxygen environment[2,6] so that oxidation would be inevitable during the synthesis or fabrication processes. The oxidation increases surface roughness and contact resistance resulting in reduction of carrier mobility.[2] Another study showed that the oxidation process changes its electronic properties drastically.[6] Thus it is necessary to understand the oxidation mechanism and its effects.

Recent studies proposed possible equilibrium structures of oxidized phosphorene, PO_x, with various oxygen concentration values of x,[7–9] suggesting possible oxidation mechanisms involving reactive dangling bonds.[7] It was reported that the most stable structure of phosphorene oxide (PO) requires the bond breaking of the strong covalent P–P bonds,[7,8] which overcomes quite high reaction barriers. There is, therefore, no structural trait of pristine phosphorene in the most stable PO structure. On the other hand, there are some other reports on a different stable structure of PO, which retains its pristine phosphorene configuration without cleavage of P–P bonds.[9] Its stability was verified by the phonon dispersion relation showing no imaginary frequencies.[9,10] These earlier studies showed that phosphorene oxide (PO) has a direct band gap of 0.6–0.88 eV slightly smaller than that of phosphorene.[7–9] It has also been reported that the band gap of phosphorene oxide can be engineered by the degree of oxidation[8] or the intensity of the electric field.[9] It was also shown that PO has very low thermal conductivity compared to that of pristine phosphorene implying that PO would be a potential material for thermoelectric applications.[10]

On the other hand, the realization of two-dimensional (2D) Dirac fermions on solid state physics[11] has given a great deal of insight into the field of 2D materials science and topology-oriented physics. The Dirac cone which is the key concept of Dirac fermions can, however, easily be gapped with intrinsic perturbations such as spin–orbit coupling.[12,13] Recently it has been found that certain nonsymmorphic crystal symmetries can support and protect 2D Dirac fermions even under the influence of the spin–orbit coupling[14] and the symmetry-induced levels of degeneracies are one of the important issues.[15]

In this paper, we report our study on the structural, electronic, and vibrational properties of phosphorene oxides, PO_x, with x varying from 0 to 1. It is found that the structural symmetry of phosphorene gets lowered in the process of oxidation. Our electronic structure calculation reveals that the band gap increases with x being maximized near $x = 0.4$, and then decreases. It is also found that the

[a] *Department of Physics and Research Institute for Basic Sciences, Kyung Hee University, Seoul, 02447, Korea. E-mail: ykkwon@khu.ac.kr*
[b] *Korea Institute for Advanced Study, Seoul, 02455, Korea*
[c] *Institute for Basic Sciences, Daejeon, 34126, Korea. E-mail: sjwoo@ibs.re.kr*
† Present address: Univ. Grenoble Alpes, Univ. Savoie Mont Blanc, CNRS, Grenoble INP, IMEP-LAHC, 38000 Grenoble, France.

This journal is © the Owner Societies 2019

oxidation makes phosphorene active to infrared (IR) absorption with high frequency and the IR active modes are blueshifted with oxidation. This suggests that the degree of oxidation can be experimentally determined using the IR spectrum.

Although the oxidation breaks the inversion symmetry underlying the puckered structure of phosphorene, we find that two additional nonsymmorphic symmetries remain in certain structures of oxidized phosphorene, for instance, PO with $x = 1$. Such nonsymmorphic symmetries guarantee symmetry-protected degeneracies in the electronic band structure within the first Brillouin zone, especially including a four-fold degenerate Dirac point. Such symmetry-protected features are accessible with reasonable electronic doping. We further check other elements with different numbers of valence electrons such as fluorene or sodium instead of oxygen showing that such four-fold-degenerate Dirac points can be even at the Fermi level on a real solid.

2 Computational details

To identify the equilibrium structures of phosphorene oxide and investigate their structural, electronic, and vibrational properties, we carried out first-principles calculations based on density functional theory (DFT) using the Vienna ab initio simulation package (VASP).[16,17] Projector augmented wave potentials[18] were employed to describe the valence electrons. The exchange–correlation functional is treated within the generalized gradient approximation (GGA) of Perdew, Burke, and Ernzerhof (PBE).[19] The cutoff energy for the plane wave basis is chosen to be 450 eV. The Brillouin zone is sampled using a Γ-centered $30 \times 30 \times 1$ grid. We used a 2×2 supercell containing 16 phosphorus atoms and a certain number of oxygen atoms ranging from 0 to 16 in order to explore the oxidation process of phosphorene with various oxygen concentrations. To avoid the spurious inter-layer interaction, we introduced a vacuum region of 15 Å along the c axis perpendicular to the sheet. Atomic relaxations were done until the Helmann–Feynman force acting on every atom becomes smaller than 0.01 eV Å^{-1}.

The vibrational properties of some selected phosphorene oxides were evaluated using the harmonic approximation implemented in the PHONOPY package.[20] To minimize their imaginary flexural modes, we used $6 \times 6 \times 1$ and $4 \times 4 \times 1$ supercell structures for partially and fully oxidized phosphorenes, respectively. We used a dipole approximation within the density functional perturbation theory[21–24] to calculate their infrared intensities $I(\omega)$ as a function of frequency ω in terms of the oscillator strengths determined by the Born effective charge tensors and the displacement vectors:

$$I(\omega) = \sum_i \left| \sum_n \sum_j Z_{n,ij}^{*} e_{n,j}(\omega) \right|^2,$$

where the index n indicates the different atoms, i and j are the Cartesian polarization, and $Z_{n,ij}^{*}$ and $e_{n,j}(\omega)$ are the Born effective charge tensor and the normalized vibrational eigenvector corresponding to ω, respectively.

3 Results and discussion

We first investigated the binding process of oxygen atoms by producing PO_x with $0 \leq x \leq 1$. Various oxygen binding sites were considered on phosphorene as shown in Fig. 1(a), where each phosphorus atom has sp^3-like bonding character with three nearest P atoms and a lone pair forming a puckered structure consisting of two P planes. Three P–P bonds can be categorized into two types, two in-plane bonds and one inter-plane bond. It was found that the lone pair binding site is more stable than any other binding site with the binding energy of 2.14 eV. We further perform the oxygen binding process by increasing the oxygen concentration x. For each oxygen concentration, there are several configurations with different oxygen distributions. Among all such possible configurations, we were able to identify the equilibrium structure. Fig. 1(b) and (c) are the equilibrium structures of PO_x with $x = 0.5$ and $x = 1$, respectively. As oxidation proceeds, both in-plane and inter-plane P–P bonds get elongated from 2.22 Å to 2.34 Å, and from 2.25 Å to 2.29 Å, respectively, as shown in Fig. 1(a)–(c). All the

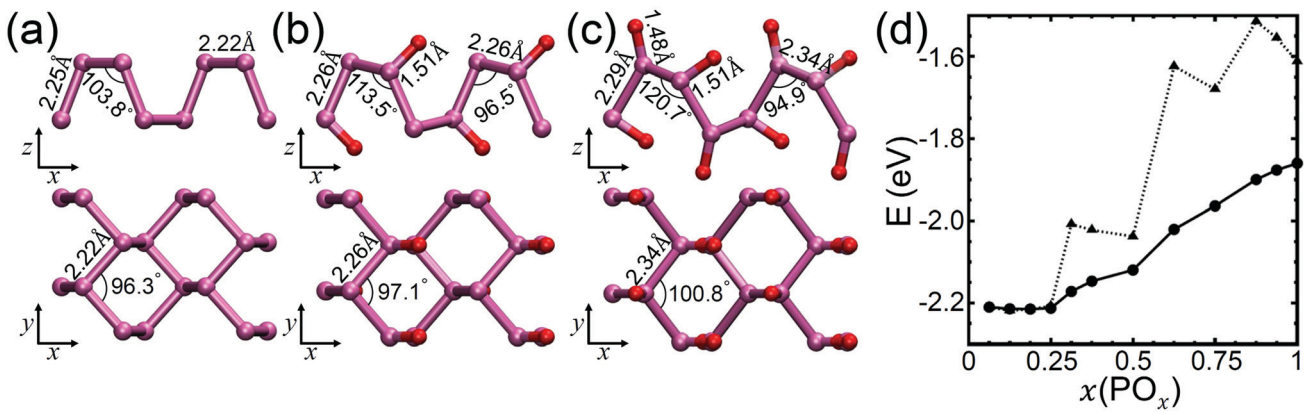

Fig. 1 Side and top views of optimized structures in a $2 \times 2 \times 1$ supercell for (a) pristine phosphorene and phosphorene oxides at two specific oxygen concentrations, (b) $PO_{0.5}$, and (c) PO. Some of their bond lengths and bond angles are also given in the respective configurations. The phosphorus and oxygen atoms are depicted by pink and red colors, respectively. (d) Formation energy (solid line) and energy gain (dotted line) of PO_x as a function of the oxygen concentration x. The energy equations are given in eqn (1) and (2) in the text.

P–O bonds in $PO_{0.5}$ are equivalent with the bond length of 1.51 Å, while PO has two distinct types of P–O bonds with 1.48 Å and 1.51 Å. The bond angle between in-plane and inter-plane P–P bonds changes from 103.8° in the pristine phosphorene to either 94.9° or 120.7° in PO through 96.5° or 113.5° in $PO_{0.5}$. The bond angle between two in-plane P–P bonds gets larger, under oxidation from 96.3° for $x = 0$ to 97.1° and 100.8° for $x = 0.5$ and $x = 1$ in PO_x. The lattice constants a and b along the x and y directions of $PO_{0.5}$ (PO) get enlarged by 2.8% (11.2%) and 2.4% (9.1%), respectively. Oxidation, thus, makes a phosphorene distorted and expanded. Our calculated PO structures agree well with a previous study[9] in terms of bond lengths and angles only within 1 to 2%.

To confirm whether the oxidation process naturally occurs in the oxygen environment, we calculated the formation energy and the energy gain as a function of oxygen concentration shown in Fig. 1(d). The formation energy $E_f(n)$ with the number of added oxygen atoms n corresponding to $x = n/16$ in the 2×2 supercell containing 16 P atoms is defined by

$$E_f(n) = \frac{1}{n}\left[E_{PO}(n) - \left(E_P + \frac{n}{2}E_{O_2}\right)\right], \quad (1)$$

where $E_{PO}(n)$ and E_P are the total energies of PO with n oxygen atoms and phosphorene in the supercell used, and E_{O_2} that of an oxygen molecule. Although the absolute values of the formation energy decrease as the oxygen concentration increases, the formation energy remains negative up to $x = 1$ indicating that the oxidation is energetically preferred. Since the formation energy, however, may not guarantee successive oxidation steps, we also computed the energy gain $\Delta E(n)$ with $x = n/16$ for every oxidation step from $n - 1$ to n, which is defined by

$$\begin{aligned}\Delta E(n) &= E_{PO}(n) - \left[E_{PO}(n-1) + \frac{1}{2}E_{O_2}\right] \\ &= nE_f(n) - (n-1)E_f(n-1).\end{aligned} \quad (2)$$

As shown in Fig. 1(d), the energy gain also remains negative verifying that the oxidation can successively progress one oxygen atom by one. It is noted that there are some other studies reporting a PO structure that is more stable than those in our study in terms of the binding energy.[7,8] Our calculation also verified that such a reported structure indeed has lower binding energy, but we found that the energy barrier to reach such a structure through an oxidation process is much higher than the structure in our study because such oxidation process must involve breaking of strong covalent bonds between phosphorus atoms. In this study, therefore, we concentrated only on the oxidation processes that break no P–P bonds.

To verify the structural stability of phosphorene oxides, we computed the phonon dispersion relations of P, $PO_{0.5}$, and PO, as shown in Fig. 2(a)–(c). Absence of negative values in the phonon frequencies indicates dynamical stability for all three configurations. All phonon frequencies of the pristine phosphorene are smaller than 500 cm^{-1} as shown in Fig. 2(a). There is, on the other hand, a nearly-flat phonon band with a higher frequency of 1100 cm^{-1} in $PO_{0.5}$ displayed in Fig. 2(b), corresponding to the stretching vibration of the P–O bond shown in Fig. 1(b). Fig. 2(c) shows two phonon flat bands with higher frequencies of 1100 cm^{-1} and 1200 cm^{-1} indicating vibration modes from two distinct P–O bonds depicted in Fig. 1(c). The higher frequency mode corresponds to the shorter bond length. Overall, our calculated phonon dispersion relations of phosphorene and PO are in good agreement with other studies.[9,10,25] The small difference observed in the PO vibrational spectrum compared to Wang *et al.*[9] was ascribed to the small structural differences mentioned above.

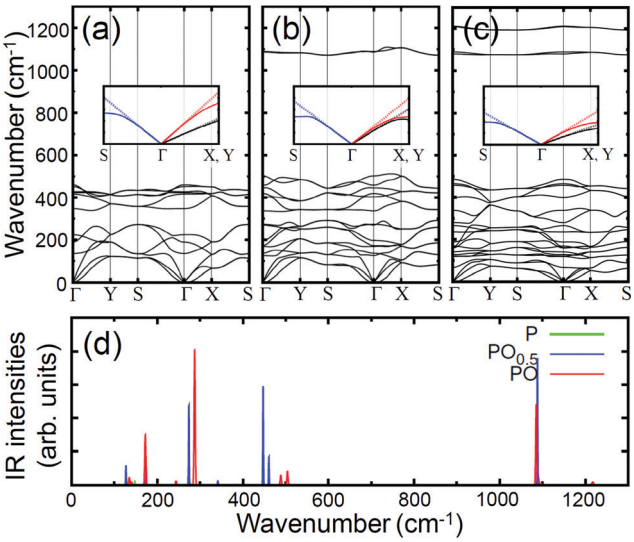

Fig. 2 Phonon dispersion relations of (a) pristine phosphorene, (b) $PO_{0.5}$, and (c) PO. Each inset displays the longitudinal acoustic branches (solid lines) near the Γ point along the three directions from the Γ point toward the S (blue), X (black) and Y (red) points and their corresponding slopes (dotted lines) at the Γ point indicating the speeds of sound, whose values are summarized in Table 1. (d) Infrared spectra of phosphorene (green) and phosphorene oxides, $PO_{0.5}$ (blue), and PO (red).

We further investigate the in-plane stiffness by computing sound velocities corresponding to the slopes of the longitudinal acoustic (LA) branches near Γ,[25] as shown in the insets of Fig. 2(a)–(c). The evaluated speeds of sound are summarized in Table 1. It clearly shows significant anisotropy in rigidity as expected from the strong anisotropic puckered structures. For all three configurations, the speeds of sound along the Γ–Y direction are much higher than along the Γ–X direction well matched with their directional rigidity. Our results also indicate that the oxidation process usually makes the LA modes softened with an exception that the LA frequencies along the Γ–X are higher in $PO_{0.5}$ than in P.

From the phonon calculations, we also computed the IR-active modes of the three optimized configurations of PO_x with $x = 0$,

Table 1 Speeds of sound along the Γ–X, Γ–Y, and Γ–S directions of P, $PO_{0.5}$, and PO evaluated from the insets in Fig. 2(a)–(c). Values are given in the units of km s^{-1}

Sound velocity	P	$PO_{0.5}$	PO
$v_{\Gamma-X}$	4.2	5.7	3.3
$v_{\Gamma-Y}$	8.4	7.5	5.4
$v_{\Gamma-S}$	7.6	7.0	5.2

This journal is © the Owner Societies 2019

0.5, and 1. Fig. 2(d) shows our calculated IR intensities. For pristine phosphorene, there is only one weak peak at 148 cm^{-1} corresponding to an out-of-plane mode. Their counter peaks for $PO_{0.5}$ and PO are observed at 127 cm^{-1} and 134 cm^{-1}, respectively. Oxidation generated other IR-active modes related to collective motions mainly by the phosphorus atom at 173 cm^{-1}, 274 cm^{-1}, 342 cm^{-1}, 448 cm^{-1}, and 462 cm^{-1} for $PO_{0.5}$, and at 173 cm^{-1}, 243 cm^{-1}, 287 cm^{-1}, 488 cm^{-1}, and 506 cm^{-1} for PO. It turns out that the P–O bond stretching modes observed in Fig. 2(b) and (c) are also IR-active around 1100 cm^{-1} for $PO_{0.5}$ and around 1100 cm^{-1} and 1200 cm^{-1} for PO. We suggest that IR measurement could possibly be used to determine the degree of oxidation of phosphorene in the experiments.

Next, we looked into the electronic band structures of various configurations of PO_x. As shown in Fig. 3(a)–(c), the pristine phosphorene and PO are semiconductors with direct band gaps of 0.88 and 0.83 eV, respectively, observed at the Γ point. On the other hand, $PO_{0.5}$ exhibits much wider band gap ($\sim$1.68 eV) than the pristine phosphorene. Moreover the band gap is indirect since the conduction band minimum moves from the Γ toward the X point, while the valence band maximum stays at Γ as shown in Fig. 3(a)–(c). Fig. 3(d) shows the trend of the band gap of PO_x with x. It tends to increase with x up to $x \simeq 0.4$ and then to decrease with x. The figure also displays the band gaps of various less stable configurations, such as those with oxygen atoms adsorbed on only one surface side. There may be some experimental conditions, such as oxidation processes of phosphorene on a substrate, where those less stable configurations would exist. Although the band gap and band dispersion are not exactly the same as those in previous work due to the slight difference in bond lengths and angles mentioned above,[9] the characteristics of band degeneracy due to crystal symmetries are the same since they belong to the same crystal symmetry group.

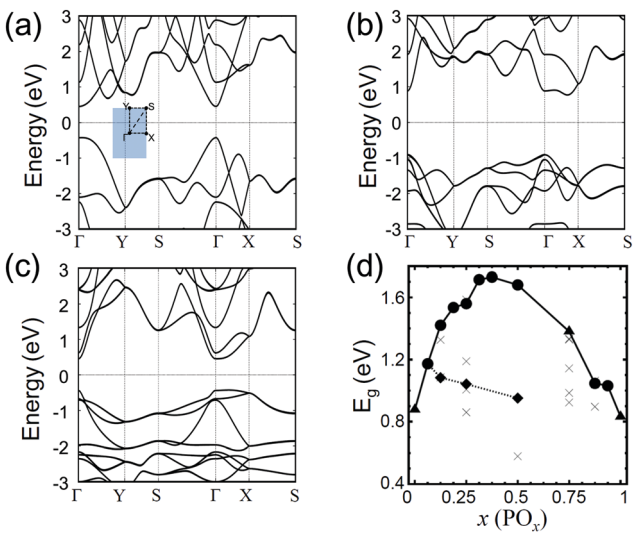

Fig. 3 Electronic band structures of (a) pristine phosphorene, (b) $PO_{0.5}$, and (c) PO. The inset shows the first Brillouin zone with the special points and lines. (d) The trend of energy gap E_g of phosphorene oxides PO_x with x, the oxygen composition. Data points connected with the solid lines correspond to E_g of the most stable PO_x for given x. The ● (▲) symbol indicates an indirect (a direct) band gap. The ♦ symbol connected with the dotted lines represents E_g of PO_x with oxygen adsorbed on only one surface side. The energy band gaps of other less stable configurations are marked with the × symbols for different x values.

The electronic structures can be characterized further by symmetry.[14,15,26] Phosphorene possesses inversion symmetry guaranteeing that its band lines are all doubly degenerate. The oxidation process usually reduces symmetries, such as the inversion symmetry breaking, and thus lifts some degeneracies in $PO_{0.5}$ and PO. It is, however, worth noting that there are two nonsymmorphic symmetries remaining in the optimized structures of both $PO_{0.5}$ and PO as shown in Fig. 1(b) and (c).

The two nonsymmorphic symmetries underlying in PO_x, which are characterized by the $\mathscr{S}$crew axis and $\mathscr{G}$lide plane, can be decomposed into products of point and translation group operations as $\mathscr{S} = C_{2x}T_{a\hat{x}/2}$ and $\mathscr{G} = M_zT_{(a\hat{x}+b\hat{y})/2}$. For a proper nonsymmorphic symmetry, the point group operator should commute with the translational partner. Here, C_{2x} and M_z are the two-fold rotation around the x axis and the mirror operation about the xy plane, respectively. $T_{\mathbf{R}}$ is the translation by the amount of $\mathbf{R}$ and a and b are the lattice constants along the x and y axes. The representation of $T_{\mathbf{R}}$ for a Bloch state with $\mathbf{k}$ is $T_{\mathbf{R}} = e^{i\mathbf{k}\cdot\mathbf{R}}$ so that

$$\mathscr{S} = C_{2x}e^{ik_xa/2} \quad \text{and} \quad \mathscr{G} = M_ze^{i(k_xa+k_yb)/2}.$$

Furthermore, for a spin-half electron, the spinor representations of C_{2x} and M_z are given by

$$C_{2x} = i\sigma_x \otimes R_x(\pi) \quad \text{and} \quad M_z = i\sigma_z \otimes R_z(\pi)P,$$

where, σ_i is the i-th component of Pauli spin matrices; $R_i(\phi)$ and P are, respectively, a real space rotation around the i-th axis by an angle ϕ and an inversion $\mathbf{r} \rightarrow -\mathbf{r}$. We use the fact that a mirror operation is a multiple of two operations, an inversion followed by a π-rotation, and that the representation of an inversion in the spin-half space is the identity. The existence of these two nonsymmorphic symmetries protect certain degeneracies and band crossing features even in phosphorene oxides without inversion symmetry. Such symmetry protected features are doubly-degenerate bands along the Γ–X and X–S lines and a four-fold degenerate Dirac point at the X point, as shown below. The bottom line is that there are two different types of guaranteed degeneracies in our system; a symmetric antiunitary operator, whose square is a negative one, guarantees degeneracy of one type[27] while two symmetric operators that anticommute mutually also guarantee further degeneracy of the other.[26]

With the symmetry under time reversal operation, Θ, one can introduce another symmetry operation, $\tilde{\Theta}$, by combining $\mathscr{S}$ with Θ such as $\tilde{\Theta} \equiv \mathscr{S}\Theta$. Let us note that Θ commutes with all spatial transformations including $\mathscr{S}$, and its square is -1 for a spin-half particle. Since the square of C_{2x} is also -1 for a spin-half particle, the square of $\tilde{\Theta}$, then, becomes

$$\tilde{\Theta}^2 = \mathscr{S}^2\Theta^2 = \left(C_{2x}e^{ik_xa/2}\right)^2\Theta^2 = e^{ik_xa}.$$

Here, it is also used that C_{2x} commutes with $e^{ik_xa/2}$. It is important to note that $\tilde{\Theta}^2$ becomes -1 at $k_x = \pi/a$, a zone boundary. From the theorem stating that any two-fold degeneracy must be protected by a symmetry that has an antiunitary operator with its square being -1,[27] the symmetry under $\tilde{\Theta}$ guarantees Kramers degeneracy between $|\psi\rangle$ and $|\tilde{\Theta}\psi\rangle$ if $|\psi\rangle$ is

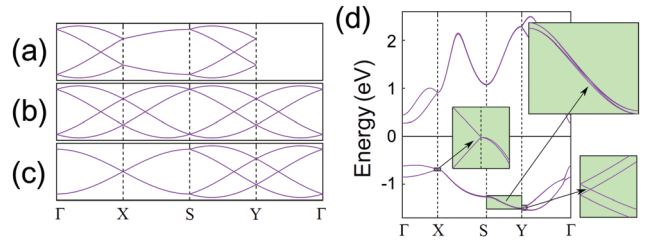

Fig. 4 Schematic band structures showing the essential level crossings, partner exchange, and symmetry protected degeneracies due to (a) $\mathscr{S} = C_{2x}T_{a\hat{x}/2}$, (b) $\mathscr{G} = M_zT_{(a\hat{x}+b\hat{y})/2}$, and (c) combined symmetries. (d) Electronic band structure of real PO replotted from Fig. 3(a), containing only eight energy bands with four below and four above the Fermi level. It exhibits all the symmetry-protected features in (c) indicating the same topological symmetry as in (c). Insets are added in order to make the detailed features visible. The same features can also be observed in the four conduction bands, although it appears as if the bands were degenerate along the *X*–*S* and *S*–*Y* lines.

a Bloch eigenstate with $k_x = \pi/a$. Note that if A is an antiunitary operator, then $\langle f|g\rangle = \langle Ag|Af\rangle$ for all vectors $|f\rangle$ and $|g\rangle$ in Hilbert space. Thus the antiunitary operator $\tilde{\Theta}$ transforms

$$\langle\psi|\tilde{\Theta}\psi\rangle = \langle\tilde{\Theta}(\tilde{\Theta}\psi)|\tilde{\Theta}\psi\rangle = \langle\tilde{\Theta}^2\psi|\tilde{\Theta}\psi\rangle.$$

Since $\tilde{\Theta}^2 = -1$ at $k_x = \pi/a$, we get $\langle\psi|\tilde{\Theta}\psi\rangle = -\langle\psi|\tilde{\Theta}\psi\rangle$, resulting in $\langle\psi|\tilde{\Theta}\psi\rangle = 0$. Since the invariant space under the operation of $\tilde{\Theta}$ is $k_x = 0$ and $k_x = \pi/a$, the band should be two-fold degenerate if $k_x = \pi/a$. It corresponds to the *X*–*S* line.

Together with the fact that there should be Weyl points on the *Γ*–*X* and *S*–*Y* lines due to the symmetry under $\mathscr{S}$,[14] the electronic structures with four bands should schematically look like Fig. 4(a). On the other hand, the symmetery under $\mathscr{G}$ guarantees nodal lines that enclose the *X* and *Y* points.[14] As a result, the band lines should look like Fig. 4(b). The only way to let such two conditions be satisfied simultaneously is to make the bands two-fold degenerate along the *X*–*S* line with the *X* point four-fold degenerate.

We have also noted a certain condition in $\mathbf{k}$ under which $\mathscr{S}$ and $\mathscr{G}$ anticommute to each other, which gives aforementioned further degeneracy in the band structure. The anticommutator between $\mathscr{S}$ and $\mathscr{G}$ becomes

$$\begin{aligned}\{\mathscr{S},\mathscr{G}\} &= i\sigma_x i\sigma_z \otimes R_x(\pi)e^{ik_xa/2}R_z(\pi)Pe^{i(k_xa+k_yb)/2} + i\sigma_z i\sigma_x \otimes R_z(\pi)Pe^{i(k_xa+k_yb)/2}R_x(\pi)e^{ik_xa/2}\\ &= i\sigma_y \otimes \left(R_x(\pi)R_z(\pi)Pe^{ik_xa/2}e^{i(k_xa+k_yb)/2} - R_z(\pi)PR_x(\pi)e^{i(k_xa-k_yb)/2}e^{ik_xa/2}\right)\\ &= -2\sigma_y \otimes R_x(\pi)R_z(\pi)Pe^{ik_xa}\sin(k_yb/2).\end{aligned}$$

Here, we have used $R_i(\pi)k_j = (-1)^{1-\delta_{ij}}k_jR_i(\pi)$ and $Pk_j = -k_jP$. It is then obvious that $\{\mathscr{S},\mathscr{G}\} = 0$ if $k_y = 0$, which guarantees two-fold degeneracy along the *Γ*–*X* line.‡

‡ Let $|k_x,+\rangle$ be an eigenstate of $\mathscr{S}$ with $k_y = 0$ and an eigenvalue $+e^{ik_xa/2}$ which is a simultaneous eigenstate of the Hamiltonian, $\mathscr{S}|+\rangle = +e^{ik_xa/2}|k_x,+\rangle$. From the anticommutity of $\mathscr{S}$ and $\mathscr{G}$, $\mathscr{S}\mathscr{G}|k_x,+\rangle = -\mathscr{G}\mathscr{S}|k_x,+\rangle = -e^{ik_xa/2}\mathscr{G}|k_x,+\rangle$, which means that $\mathscr{G}|k_x,+\rangle$ is also an eigenstate of $\mathscr{S}$ with a different eigenvalue $-e^{ik_xa/2}$. Since the symmetry of the Hamiltonian under $\mathscr{G}$ guarantees that both $|k_x,+\rangle$ and $\mathscr{G}|k_x,+\rangle$ have the same energy, it proves that the states with $k_y = 0$ should be doubly degenerate. It corresponds to the *Γ*–*X* line.

Including all these factors, the band structure of a system symmetric under $\mathscr{S}$ and $\mathscr{G}$ should be doubly degenerate along the *Γ*–*X*–*S* line with a four-fold degeneracy at the *X* point [Fig. 4(c)]. Such a four-fold degenerate Dirac point is protected even with spin–orbit coupling properly taken into account and can be accessed with moderate doping for PO. Fig. 4(d) shows the band structure of PO from our *ab initio* calculations, which contain all the essential features described in the schematic one shown in Fig. 4(c). A final remark we would like to mention is that the same kind of Dirac point can be realized even at the Fermi level by replacing the oxygen atoms for $PO_{0.5}$ with atoms of odd number of valence electrons such as fluorine or sodium making such materials essentially metallic. Although a systematic stability check for $PF_{0.5}$ and $PNa_{0.5}$ is beyond the scope of this work, we have confirmed numerically that there is no negative phonon frequencies with the structures of the same symmetry as $PO_{0.5}$.

4 Conclusions

We presented the structural, electronic, and vibrational properties of phosphorene oxides PO_x with $x \in [0,1]$ using *ab initio* density functional theory. Our calculated formation energy and energy gain showed that the oxidation occurs naturally at least up to $x = 1$. Moreover, calculated phonon dispersion relations confirm that there is no imaginary frequency, verifying that phosphorene oxides are structurally stable. We also proposed that the degree of oxidation might be probed using IR analysis. The electronic band gap increases with oxidation with x for $x \lesssim 0.4$ and then decreases. The most intriguing result in this report is that two nonsymmorphic symmetries guarantee symmetry-protected degeneracies in the electronic band structures including a four-fold degenerate Dirac point accessible with moderate doping.

Conflicts of interest

There are no conflicts to declare.

Acknowledgements

We acknowledge financial support from the Korean government through National Research Foundation (2019R1A2C1005417). Some portion of our computational work was done using the resources of the KISTI Supercomputing Center (KSC-2018-C2-0033 and KSC-2018-CHA0052).

References

1 L. Li, Y. Yu, G. J. Ye, Q. Ge, X. Ou, H. Wu, D. Feng, X. H. Chen and Y. Zhang, *Nat. Nanotechnol.*, 2014, **9**, 372–377.

 This journal is © the Owner Societies 2019

2 S. P. Koenig, R. A. Doganov, H. Schmidt, A. H. Castro Neto and B. Özyilmaz, *Appl. Phys. Lett.*, 2014, **104**, 103106.
3 H. Liu, A. T. Neal, Z. Zhu, Z. Luo, X. Xu, D. Tománek and P. D. Ye, *ACS Nano*, 2014, **8**, 4033–4041.
4 Z. Guo, H. Zhang, S. Lu, Z. Wang, S. Tang, J. Shao, Z. Sun, H. Xie, H. Wang, X.-F. Yu and P. K. Chu, *Adv. Funct. Mater.*, 2015, **25**, 6996–7002.
5 A. Castellanos-Gomez, L. Vicarelli, E. Prada, J. O. Island, K. L. Narasimha-Acharya, S. I. Blanter, D. J. Groenendijk, M. Buscema, G. a. Steele, J. V. Alvarez, H. W. Zandbergen, J. J. Palacios and H. S. J. van der Zant, *2D Mater.*, 2014, **1**, 025001.
6 J. O. Island, G. A. Steele, H. S. J. V. D. Zant and A. Castellanos-gomez, *2D Mater.*, 2015, **2**, 011002.
7 A. Ziletti, A. Carvalho, D. K. Campbell, D. F. Coker and A. H. C. Neto, *Phys. Rev. Lett.*, 2015, **114**, 046801.
8 A. Ziletti, A. Carvalho, P. E. Trevisanutto, D. K. Campbell, D. F. Coker and A. H. C. Neto, *Phys. Rev. B: Condens. Matter Mater. Phys.*, 2015, **91**, 085407.
9 G. Wang, R. Pandey and S. P. Karna, *Nanoscale*, 2015, **7**, 524–531.
10 S. Lee, S.-H. Kang and Y.-K. Kwon, *Sci. Rep.*, 2019, **9**, 5419.
11 G. W. Semenoff, *Phys. Rev. Lett.*, 1984, **53**, 2449–2452.
12 F. D. M. Haldane, *Phys. Rev. Lett.*, 1988, **61**, 2015–2018.
13 C. L. Kane and E. J. Mele, *Phys. Rev. Lett.*, 2005, **95**, 146802.
14 S. M. Young and C. L. Kane, *Phys. Rev. Lett.*, 2015, **115**, 126803.
15 B. J. Wieder, B. Bradlyn, Z. Wang, J. Cano, Y. Kim, H.-S. D. Kim, A. M. Rappe, C. L. Kane and B. A. Bernevig, *Science*, 2018, **361**, 246–251.
16 G. Kresse, *Phys. Rev. B: Condens. Matter Mater. Phys.*, 1996, **54**, 11169–11186.
17 G. Kresse and J. Furthmüller, *Comput. Mater. Sci.*, 1996, **6**, 15–50.
18 P. E. Blöchl, *Phys. Rev. B: Condens. Matter Mater. Phys.*, 1994, **50**, 17953–17979.
19 J. P. Perdew, K. Burke and M. Ernzerhof, *Phys. Rev. Lett.*, 1996, **77**, 3865–3868.
20 A. Togo, F. Oba and I. Tanaka, *Phys. Rev. B: Condens. Matter Mater. Phys.*, 2008, **78**, 134106.
21 R. Pick, M. Cohen and R. Martin, *Phys. Rev. B: Solid State*, 1970, **1**, 910.
22 G. Kresse, J. Furthmüller and J. Hafner, *Europhys. Lett.*, 1995, **32**, 729–734.
23 S. Baroni, S. Gironcoli, A. Corso and P. Giannozzi, *Rev. Mod. Phys.*, 2001, **73**, 515–562.
24 D. Karhánek, T. Bučko and J. Hafner, *J. Phys.: Condens. Matter*, 2010, **22**, 265006.
25 Z. Zhu and D. Tománek, *Phys. Rev. Lett.*, 2014, **112**, 176802.
26 B. J. Wieder and C. L. Kane, *Phys. Rev. B*, 2016, **94**, 155108.
27 J.-M. Hou and W. Chen, *Front. Phys.*, 2018, **13**, 130301.